Supplementary Information

High photocatalytic performance over ultrathin 2D TiO_2 for CO_2 reduction to alcohols

Chenxu Yin,[a] Xue Li,[a] Shangcong Sun,[b] Xiaoqian Wei,[a] Qing Tong,[a] Wei Tan,[a] Xin Wang,[a] Bo Peng,[b*] Haiqin Wan [a*]and Lin Dong [a]

[a] *State Key Laboratory of Pollution Control and Resource Reuse, School of the Environment, Centre of Modern Analysis, Jiangsu Key Laboratory of Vehicle Emissions Control, Nanjing University, Nanjing 210023, China*

[b] *SINOPEC Research Institute of Petroleum Processing Co., Ltd. Beijing 100083, China*

Experimental Section

Catalyst preparation

Ultrathin TiO_2 nanosheets were obtained by the solvothermal method. In detail, 1 mL titanium tetrachloride was added into 30 mL ethylene glycol, and stirred at ambient temperature for 0.5 h. Afterwards, 1 mL methanol/ethanol/distilled water was dropped in the mixture, with vigorous stirring for 0.5 h. The resulting mixture was allowed to react in a 50 mL Teflon-lined autoclave at 150 ℃ for 4 h. The generated white precipitate was collected, washed with ethanol and distilled water, followed by drying at 80 ℃ for 12 h in a vacuum oven. The resulting samples were denoted as UT-M, UT-E, and UT-W.

The commercial P25 purchased from Degussa, 21 nm primary particle size (TEM), ≥99.5% trace metals basis. The ratio of anatase to rutile is about 80:20.

Catalyst characterizations

X-ray diffraction patterns (XRD) were collected on an X-ray diffractometer with Cu-kα radiation (λ = 0.154178 nm) at 40 kV and 40 mA with a scan speed of 0.5 ° min^{-1}. Atomic force microscope (AFM) measurement was performed on a Bruker Dimension Edge instrument. Transmission electron microscopy (TEM) images were obtained on a JEM-2100 microscope at an acceleration voltage of 200 kV. Dynamic Light Scattering (DLS) was performed on a Malvern zs90. The Brunauer-Emmett-Teller (BET) approach was used to evaluate the specific surface area of the samples by nitrogen adsorption-desorption test.

Surface chemistry and valence band (VB) were examined by X-ray photoelectron spectroscopy (XPS) analysis, which was performed on a PHI 5000 Versa Probe high-performance electron spectrometer using monochromatic Al Kα radiation (1486.6 eV). The binding energies were calibrated to the adventitious carbon (C 1s peak at 284.6 eV).

Thermogravimetric and differential thermal analysis (TG-DTA) was performed on a STA 449 C device from 20 ℃ to 900 ℃ with a ramping rate of 20 ℃ min^{-1} in a stream of air. Fourier transform infrared (FT-IR) spectra were recorded on a NICOLET Is10 FT-IR spectrometer.

The ultraviolet-visible diffuse reflection adsorption spectra (UV-vis) was collected by an UV-

vis spectrometer (Shimadzu, UV-2401) with $BaSO_4$ as a reference and the measurement ranged from 200 to 800 nm. Photoluminescence (PL) spectra were carried out on a F-7000 fluorescence spectrophotometer (Hitachi, Tokyo, Japan) with an excitation wavelength of 325 nm at ambient temperature. The slit in all measurements was 2 nm.

In-situ electron spin resonance (in situ ESR) under the irradiation of a Xenon lamp signal was determined at 90 k by an ESR JES FA200 (JEOL) spectrometer, purged with CO_2 (purity＞99.999 %) to raise the CO_2 pressure to 0.2 MPa, which was used to obtain the signal of DMPO-$\cdot CO_2^-$ at different irradiation time. The aqueous solution of DMPO (5,5-dimethyl-1-pyrroline N-oxide) served as the trapping agent.

The electron spin resonance (EPR) under the dark and N_2 atmospheres at the ambient temperature was used to obtain the signal of oxygen vacancies.

Gas chromatography mass spectrometry (GC-MS) tests were performed on SHIMADZU GCMS-QP2020 NX equipped with WAX chromatographic column (30 m, inner diameter 0.25 mm, film thickness 0.25 μm). The injection temperature is 280 ℃. The fragment of m/z = 30.6, 32, 44, 45, 47, and 48 are assigned to $^{13}CH_3$ $^{13}CH_2$, $^{13}CH_2OH$, $^{12}CO_2$, $^{13}CO_2$, $^{13}CH_3$ $^{13}CH_2O$, and $^{13}CH_3$ $^{13}CH_2OH$ in MS results with $^{13}CO_2$ liquid products.

Photoelectrochemical measurements, including electrochemical impedance spectroscopy (EIS) and transient photocurrent response were performed on a three-electrode system electrochemical workstation (CHI 660, CHInstrument, Shanghai). Platinum wire electrode and Ag/AgCl electrode were used as counter electrode and reference electrode, respectively. The catalyst-modified ITO glass (1×1 cm^2) by dip-coating method (5 mg of sample dispersed in 50 μL of ethanol) was used as working electrode. A 300 W Xe lamp was used as the light source and Na_2SO_4 (0.25 M) as the electrolyte solution.

In-situ diffuse reflectance infrared Fourier-transform spectra (DRIFTS): The in-suit CO_2 adsorption DRIFTS was measured on a Nicolet Is50FT-IR spectrometer (Thermo Fisher, USA) with a frequency range of 1200-4000cm^{-1} and a spectral resolution of 4 cm^{-1} (scanning times: 32). The spectrometer was equipped with a specimen chamber and a highly sensitive mercury cadmium telluride (MCT) detector, cooled by liquid N_2. In a typical process, the CO_2 adsorption experiments were conducted as follows: the catalysts were put in the chamber, which was sealed and purging with N_2 for 1.5 h at 120 ℃. The background signal was collected during N_2 flow. Then the CO_2 gas

and H_2O vapors were switched into the system to collect CO_2 adsorption signal interval of 2 min until equilibrium. Finally, the Xe lamp was switched on to initiate the reaction, and the in suit FTIR spectra were collected by an MCT detector. The typical signals of diverse intermediates were detected subsequently after the flowed CO_2 and H_2O vapors under dark and light irradiation (0-30 min).

Evaluation of the catalytic performance

Standard testing

Photocatalytic CO_2 conversion experiment was carried out in an automatic reaction system with 100 cm^3 quartz beaker. In a typical experiment, 20 mg of photocatalyst and 5 mL distilled water were added into a 50 mL homemade quartz groove and sonicated for 30 min to achieve a uniform dispersion. The quartz groove was then placed in the reactor, sealed and purged with CO_2 (purity＞99.999 %) for 20 min to remove air. After raising the CO_2 pressure to 0.4 MPa, photocatalytic reaction was performed for a total of 8 h under the illumination of a 300 W Xenon lamp with the reactor kept at 20 ℃.The gas products of the reaction were detected and analyzed by gas chromatograph (GC) equipped with a flame ionization detector (FID2) and a thermal conduction detector (TCD), using Ar the carrier gas. The liquid products were detected by GC-FID1 equipped with a low polar capillary column (HF-5) (50 m×0.53 mm (ID) ×1.0 μm). In addition, the temperature of the injector, the column oven, and the FID1 detector is set to be 260, 80, and 180 ℃, respectively.

The formation rate and selectivity of products were calculated using equations presented below. Please note that O_2 was not quantified due to inevitable exposure to air during the manual injection.

$$P_{CO} = \frac{A_{CO} C_s' P V_r}{A_0 R T m_{cat}} \quad (1)$$

$$P_{CH4} = \frac{A_{CH_4} C_s'' P V_r}{A_1 R T m_{cat}} \quad (2)$$

$$P_{\text{liquid products}} = \frac{C_s''' V_s n}{m_{cat}} \quad (3)$$

A_{CO} was the CO peak area, A_{CH_4} was the CH_4 peak area, A_0 was the CO standard area, A_1 was the CH_4 standard area, C_s' was the CO standard concentration, C_s'' was the CH_4 standard concentration, C_s''' was the concentration of methanol or ethanol, P was the pressure in the reactor, V_r was the reactor volume, V_s was the volume of methanol or ethanol, R was the universal gas constant, T was the reactor temperature, m_{cat} was catalyst weight.

The electron-based selectivity of CH_3OH was calculated using equarion (4):

$$\mathrm{Sel_{electron}}(CH_3OH) = \left(\frac{n(CH_3OH) \times 6}{n(CO) \times 2 + n(CH_4) \times 8 + n(CH_3OH) \times 6 + n(C_2H_5OH) \times 12}\right) \times 100\% \quad (4)$$

The electron-based selectivity of C_2H_5OH was calculated using equation (5):

$$\mathrm{Sel_{electron}}(C_2H_5OH) = \left(\frac{n(C_2H_5OH) \times 12}{n(CO) \times 2 + n(CH_4) \times 8 + n(CH_3OH) \times 6 + n(C_2H_5OH) \times 12}\right) \times 100\% \quad (5)$$

The electron-based selectivity of liquid products was calculated using equation (6):

$$\mathrm{Sel_{eletron}}\ (\text{liquid products}) = \left(\frac{n(CH_3OH) \times 6 + n(C_5H_5OH) \times 12}{n(CO) \times 2 + n(CH_4) \times 8 + n(CH_3OH) \times 6 + n(C_2H_5OH) \times 12}\right) \times 100\% \quad (6)$$

where n is the formation rate.

The quantum efficiency at three different wavelengths (450 nm, 420 nm and 365 nm) was calculated using equation (7):

$$\mathrm{QE} = \frac{xnN_Ahc}{tPS\lambda} \times 100\% \quad (7)$$

X was the number of electrons transferred by the reaction, n was the amount of product, h was the Planck constant, c was the speed of light, t was the reaction time, P was the optical power density, S was the lighted area, λ was the wavelength of the incident light..

Recycling testing

The recycling testing was conducted as follows. After first reaction, the used catalyst was recovered by centrifugation. It was then used in the second reaction test, and so on. This is repeated for three tests.

Figure S1-S23

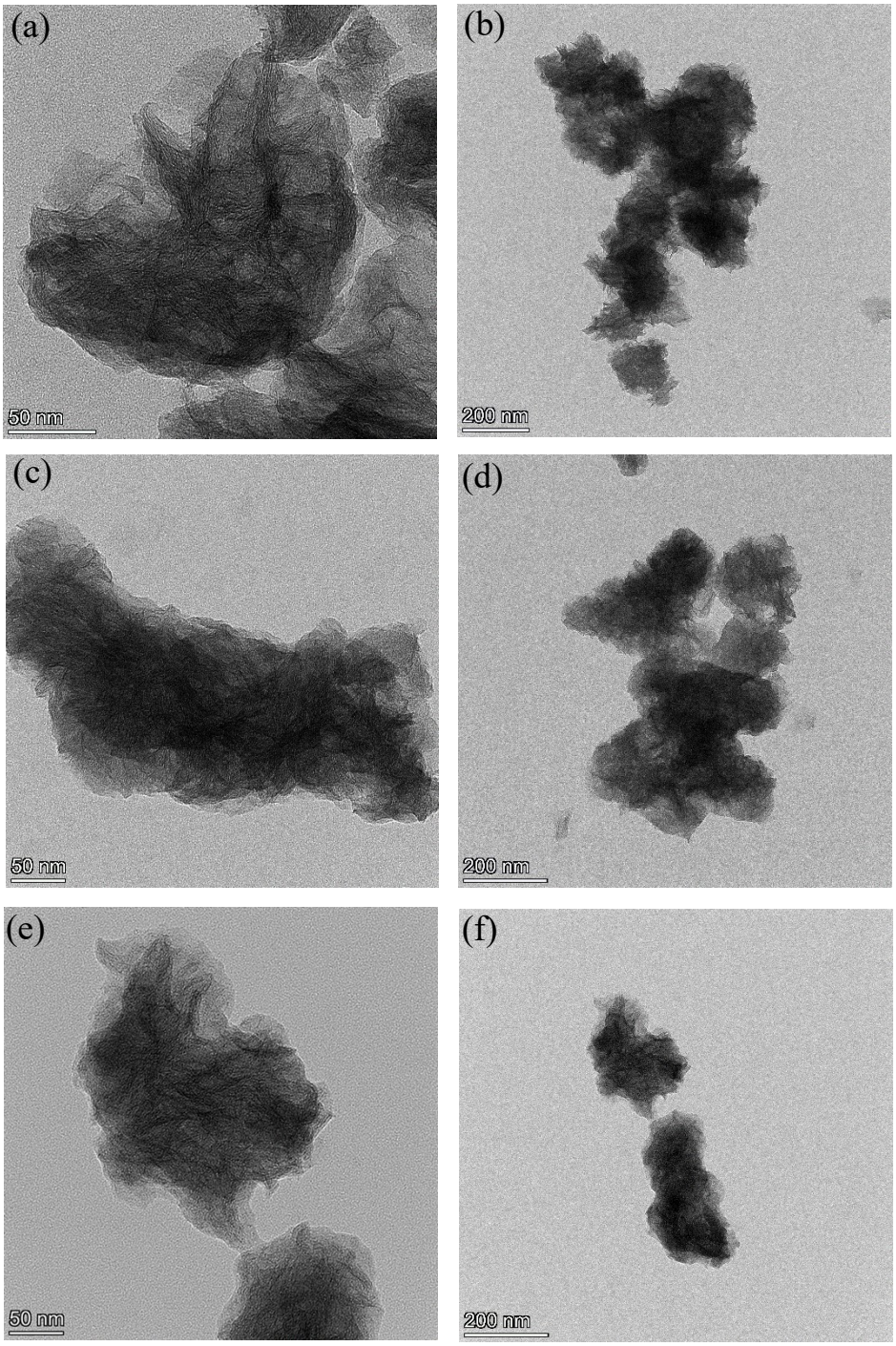

Figure S1 Morphological characterizations of three catalysts. TEM images of (a, b) UT-E, (c, d) UT-M, and (e, f) UT-W.

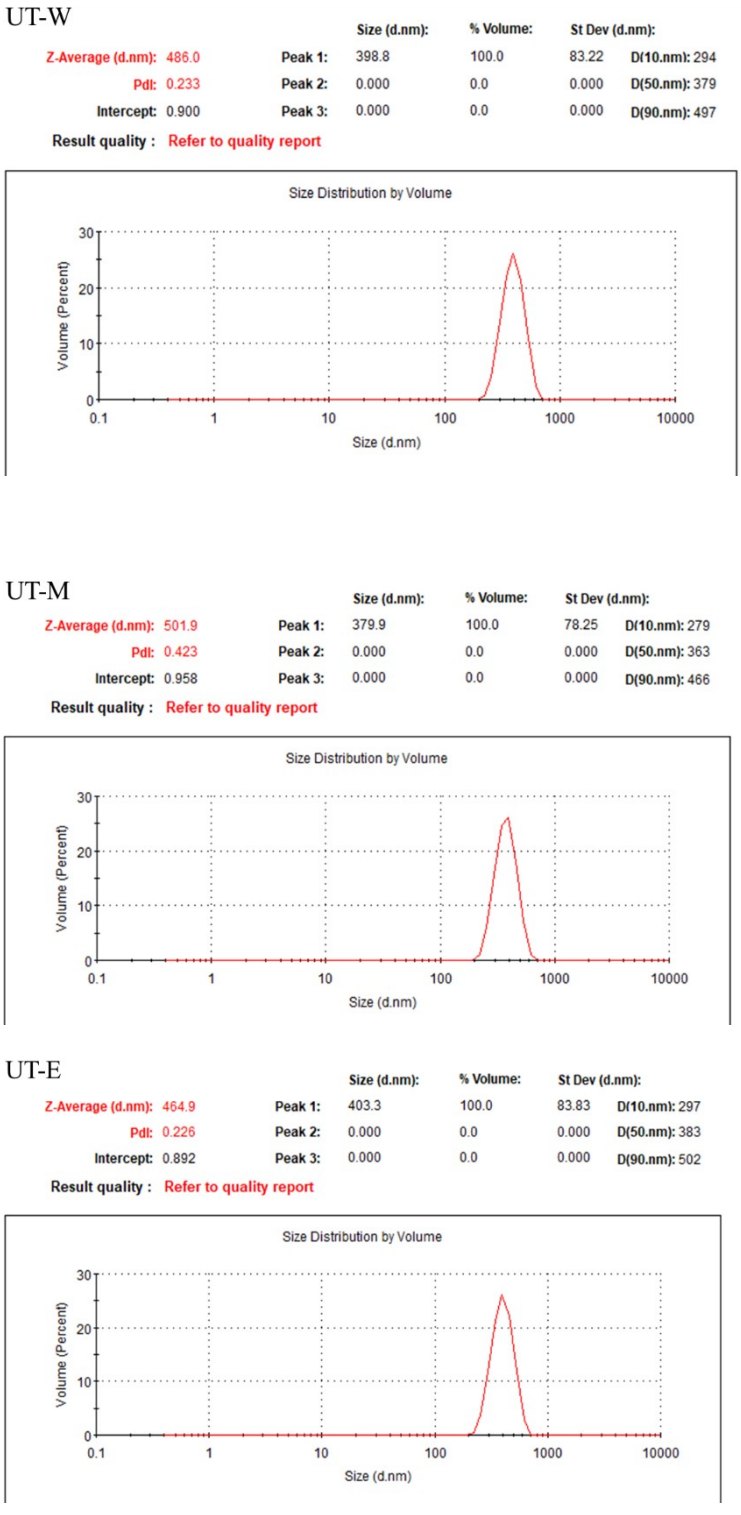

Figure S2 The DLS analysis of UT-W, UT-M, and UT-E samples, respectively.

Dynamic Light Scattering analysis conducted on the UT-W, UT-M and UT-E samples yielded an average diameter of 486.0 nm, 501.9 nm, and 464.9 nm, respectively. In fact, our nomenclature for the prepared materials is from a reference in the earlier articles synthesizing ultrathin TiO_2 nanosheets[1].

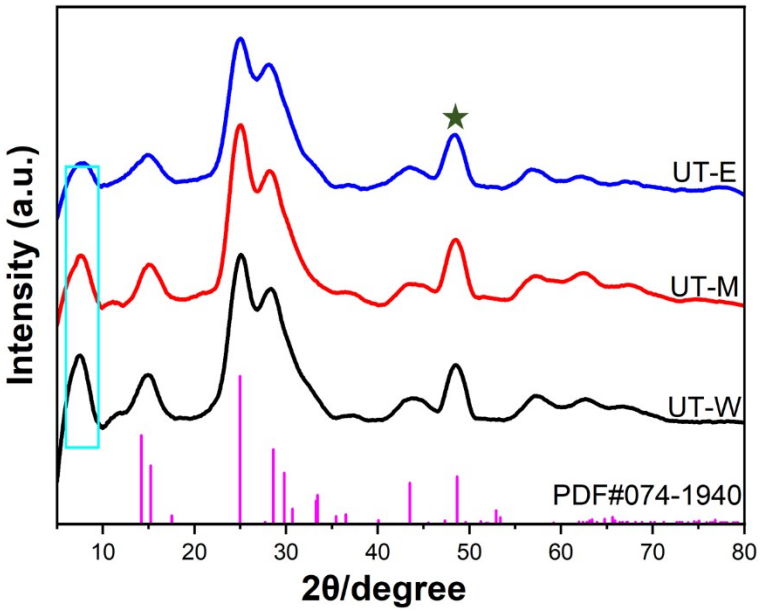

Figure S3 XRD patterns of three samples, showing a typical TiO_2(B) phase. The observed reflections showed the formation of a pure compound indexed according to the monoclinic structure to the C2/m space group.

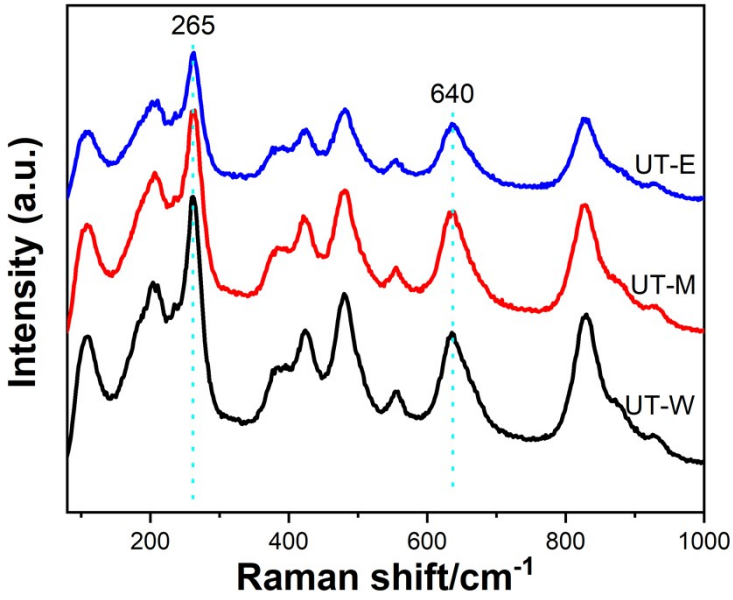

Figure S4 Raman spectra of UT-W, UT-M, and UT-E.

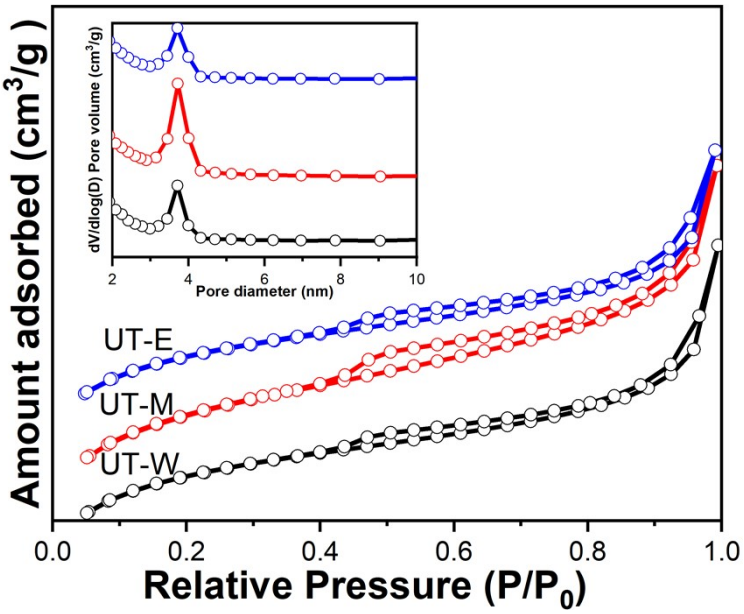

Figure S5 N_2 adsorption/desorption isotherm of the samples at 77 K. The samples were degassed at 100 °C for 8 h. All isotherms are typical IV with H3 hysteresis loops. The pore-size distributions are similar for all samples, which display a relatively wide range from 2 to 10 nm.

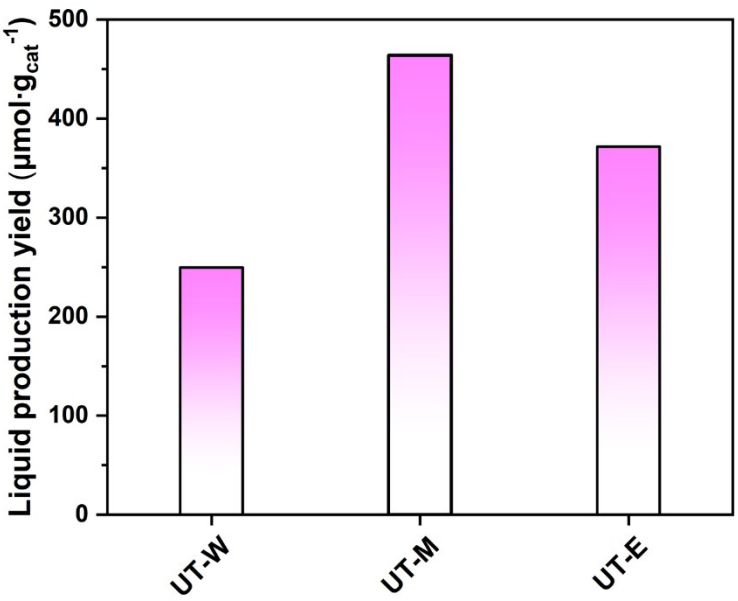

Figure S6 Formation rate of liquid products on UT-W, UT-M, and UT-E.

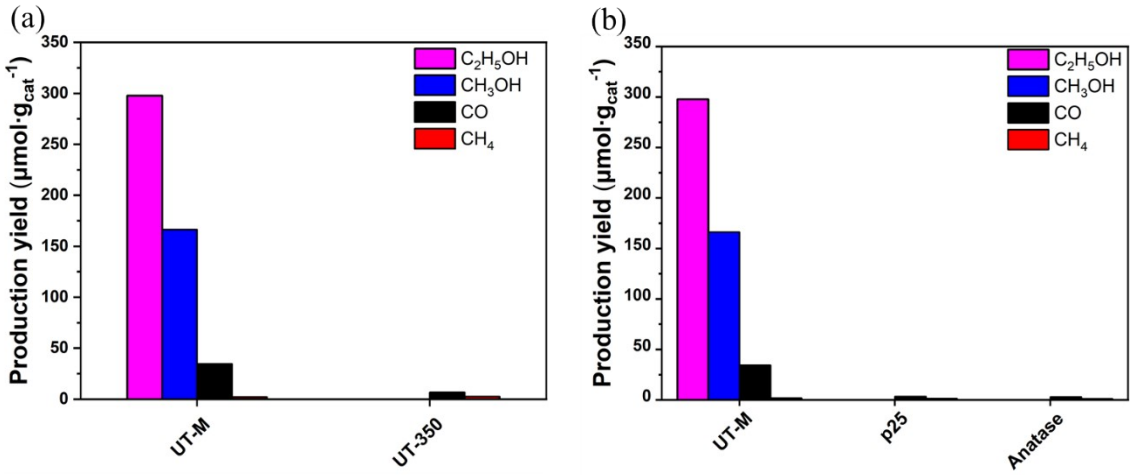

Figure S7 Control experiments: (a) UT-M and UT-350, (b) UT-M, P25, and Anatase phase TiO_2. The products towards CH_3OH, and C_2H_5OH were generated on the ultrathin TiO_2-based catalysts, indicating that the atomically thin 2D geometry is favorable for the improvement of CO_2 activity through the potential exposure of many rich active sites and a shortened charge-transfer distance from the interior to the surface.

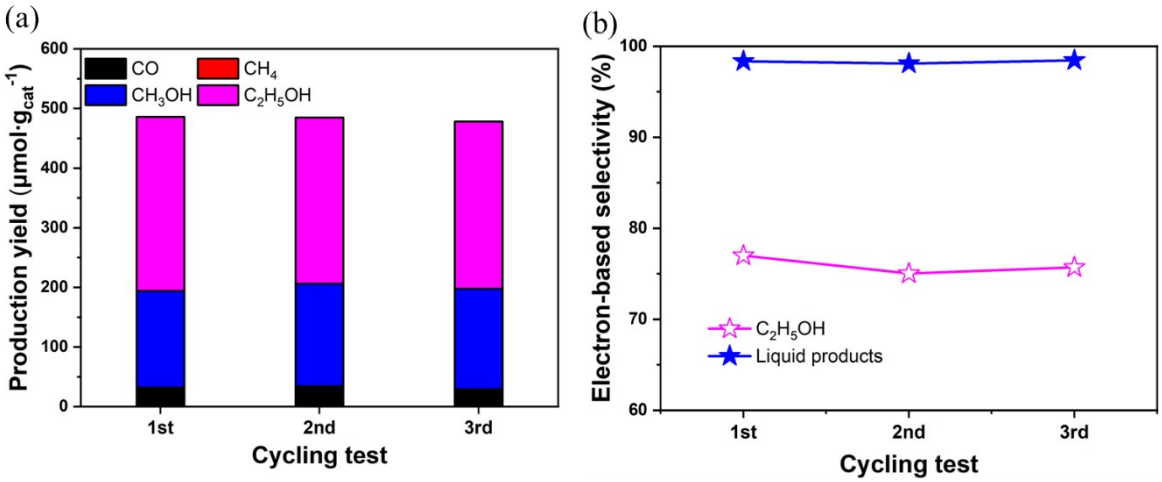

Figure S8 (a) Product formation rate and (b) electron-based selectivity on UT-M catalyst over 3 cycling tests. The electron-based selectivities towards liquid products on UT-M over 3 cycling tests are 98.4 %, 98.1 %, and 98.5 %, respectively, and those toward C_2H_5OH are 77.0 %, 75.1 %, and 75.7 %, respectively.

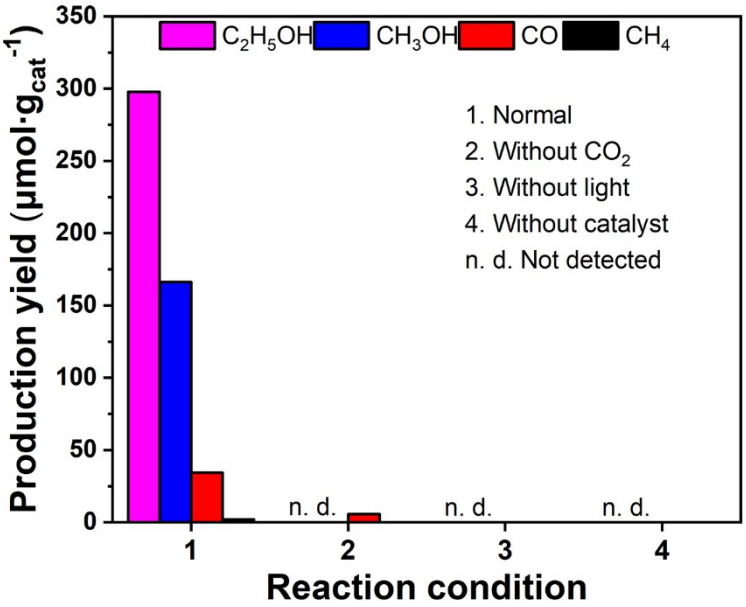

Figure S9 Control experiments under different reaction conditions for CO_2 reduction on UT-M catalyst.

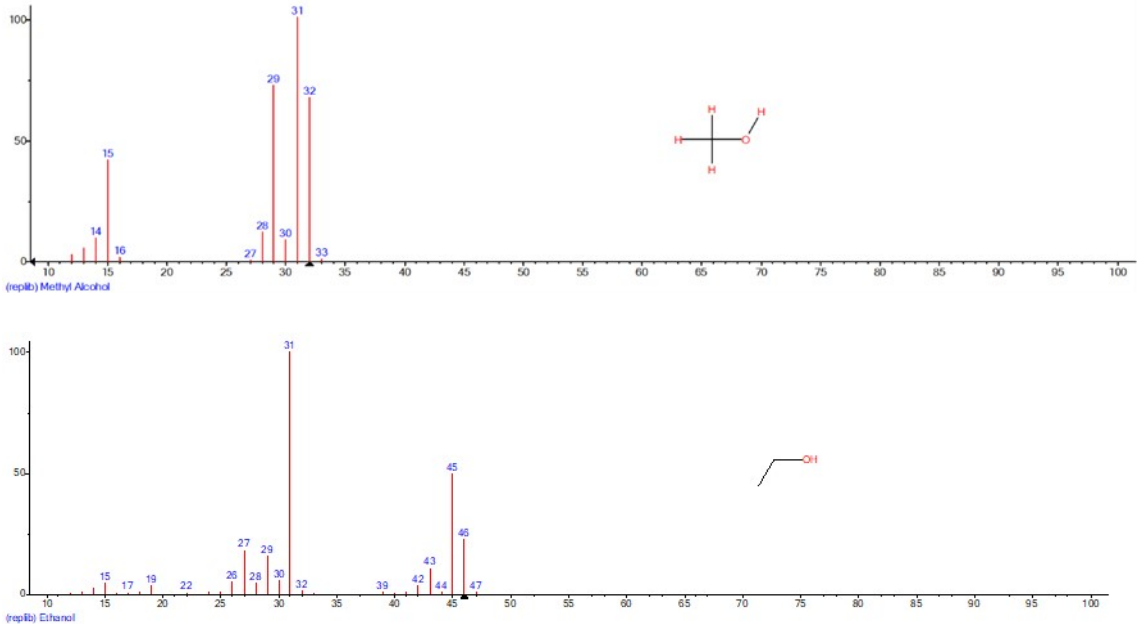

Figure S10 The ^{12}C mass chromatogram of standard methanol/ethanol substance.

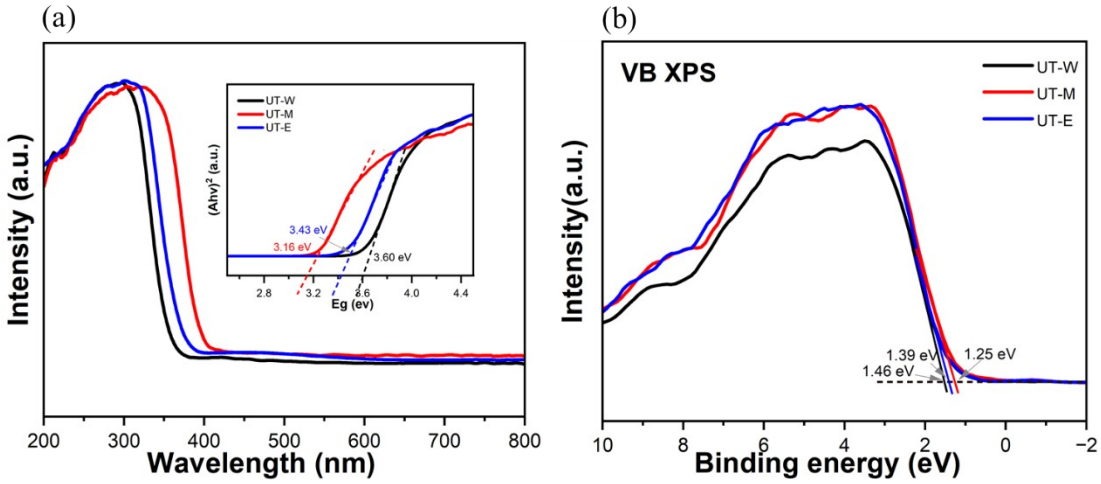

Figure S11 (a) UV−vis DRS and corresponding band edges of UT-W, UT-M, and UT-E; (b) valence band XPS spectra of UT-W, IT-M, and UT-E.

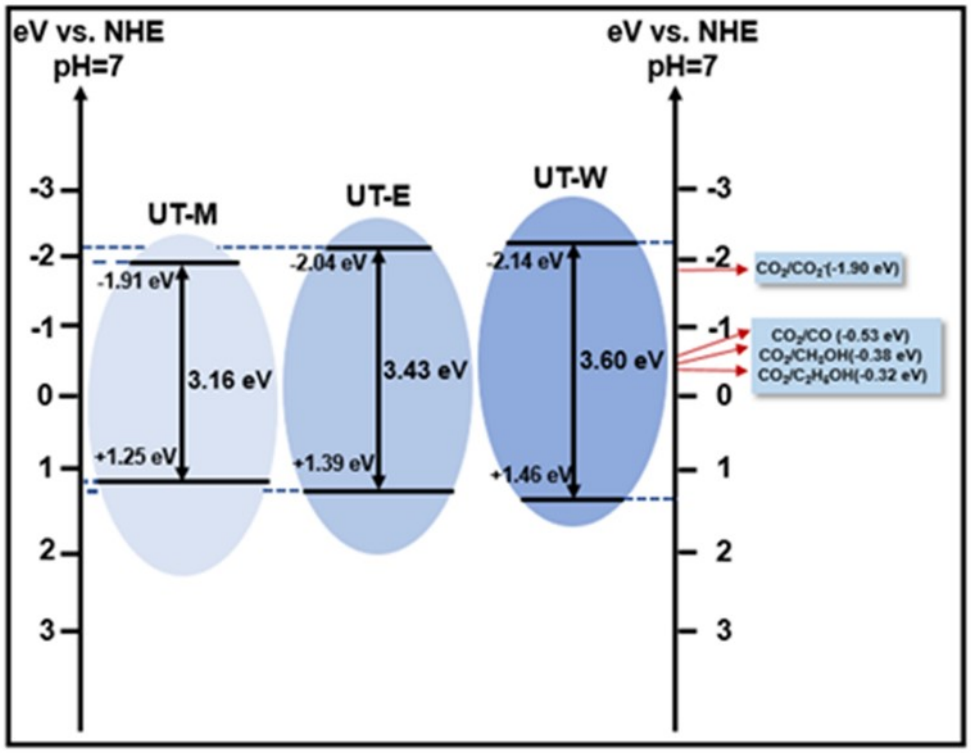

Figure S12 Band structure diagram of UT-W, UT-W, and UT-E.

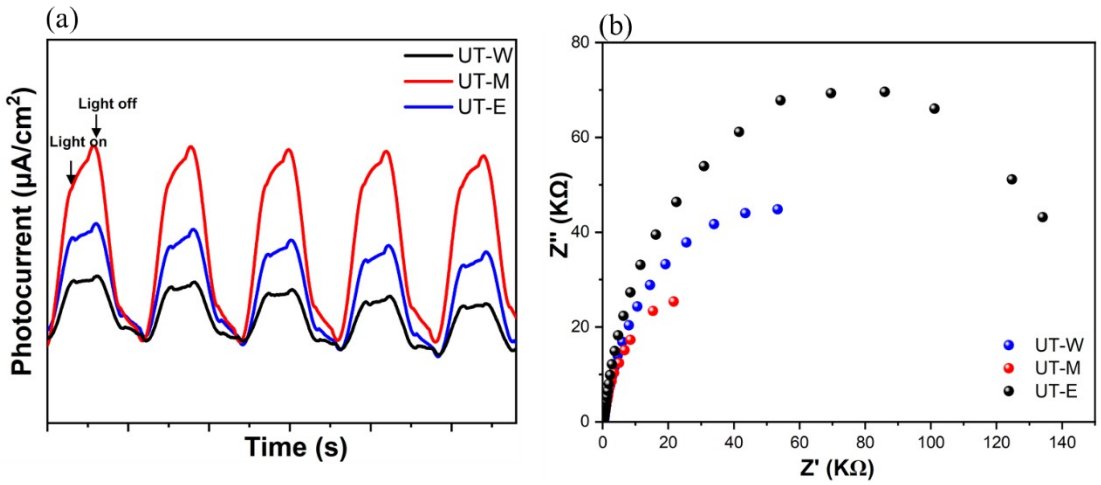

Figure S13 (a) Photocurrent-time plots and (b) EIS spectra of UT-W, UT-M, and UT-E. UT-M delivers significantly higher photocurrent than UT-E and also UT-W. Meanwhile, EIS analysis reveals that the charge transportation resistance decreases significantly from UT-E to UT-M, following the order of UT-E＞UT-W＞UT-M. This explains the high photocurrent observed in UT-M.

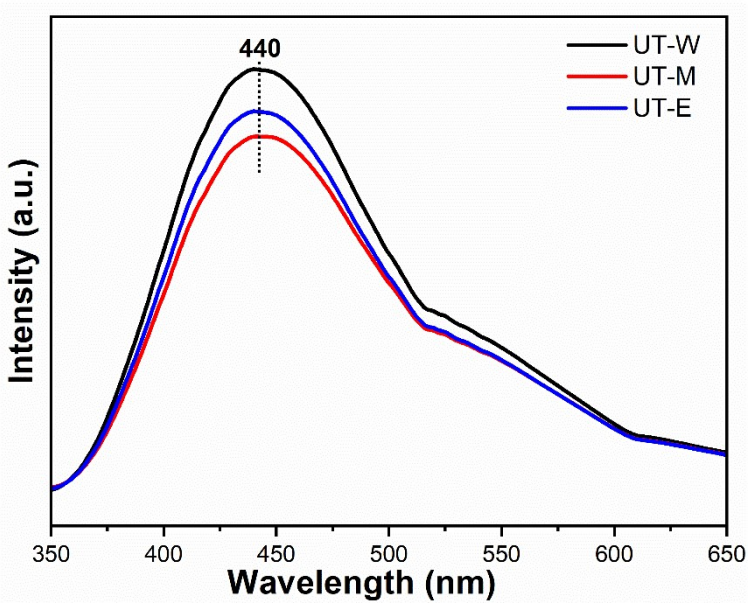

Figure S14 PL spectra taken at 325 nm excitation of UT-W, UT-M, and UT-E. Notably, UT-M displays strongest quenching effect, followed by UT-E and UT-W.

Figure S15 The water contact angle results of UT-W, UT-M, and UT-E.

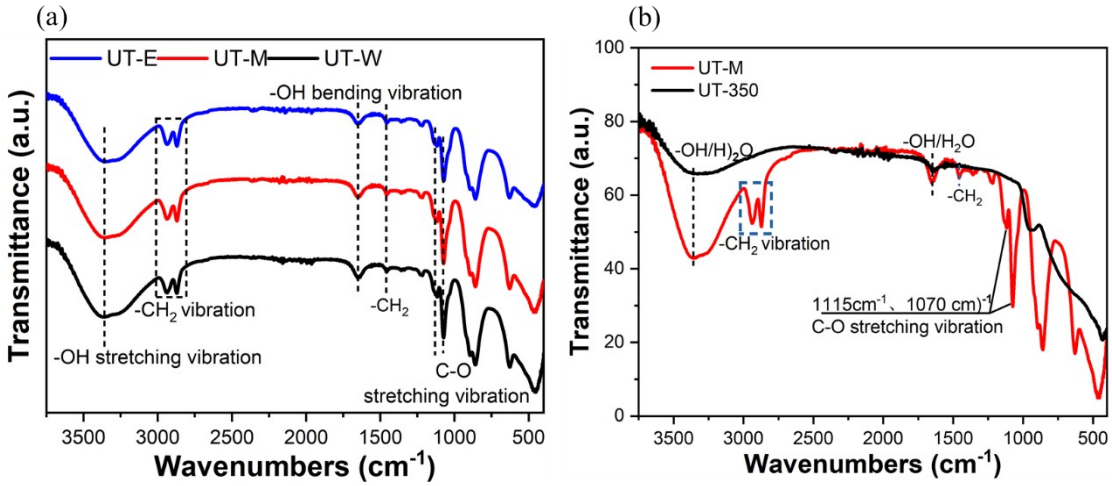

Figure S16 Infrared spectroscopy (IR) spectra of (a) UT-W, UT-M, and UT-E and (b) UT-350. Characteristic absorption bands of ethylene glycol were in presence for the samples before the calcination treatment.

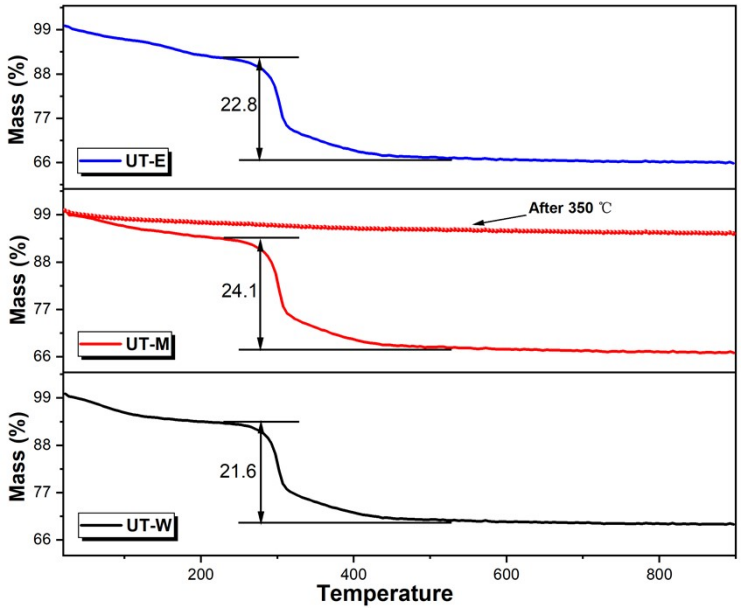

Figure S17 Thermogravimetric analysis (TGA) of UT-W, UT-M, UT-E, and UT-350. For the samples before the calcination treatment, The EG ligands on the surface accounts for ~20 wt% for as-synthesized samples. After calcination, all EG ligands on the surface were removed.

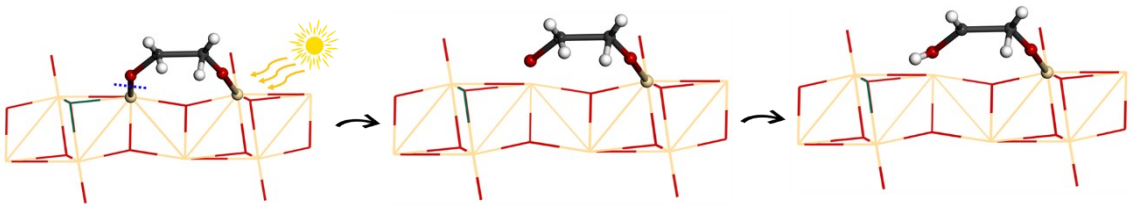

Figure S18 The formation of ethylene glycol (EG) radicals under the UV treatment.

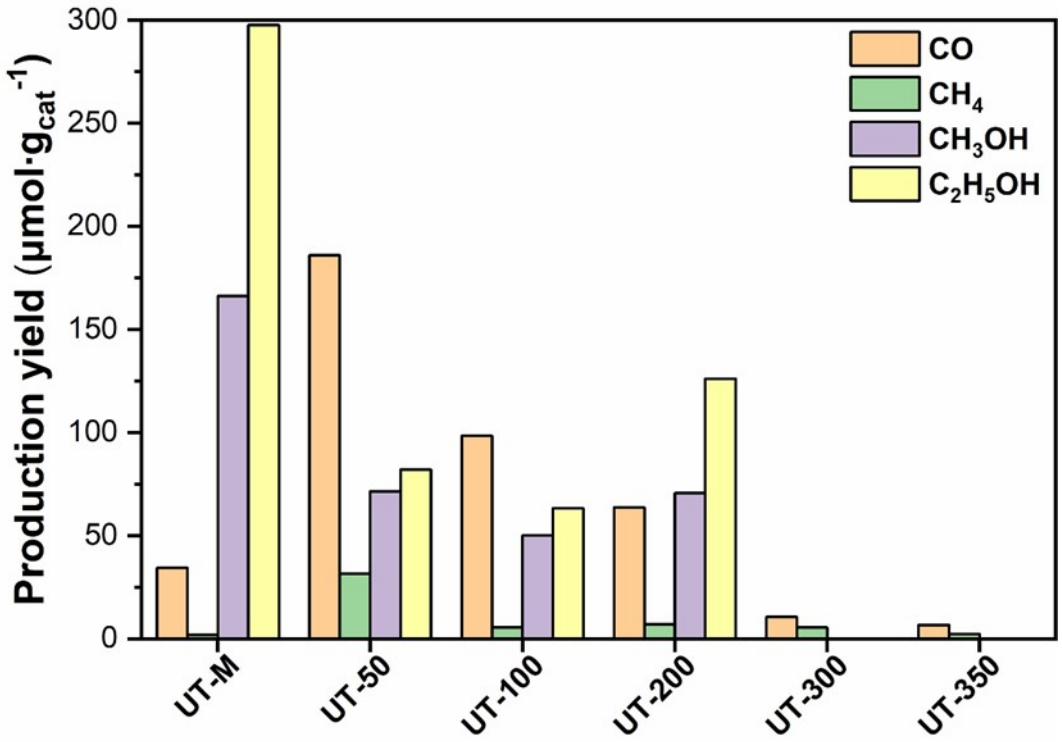

Figure S19 The activity of samples calcined at different temperatures.

After calcining at a series of different temperature in air (50 ℃, 100 ℃, 200 ℃, 300 ℃, 350 ℃), the results showed decreased activity for all samples. For the UT-300 and UT-350 samples, there are only gaseous CO and CH_4 and no liquid-phase products generated.

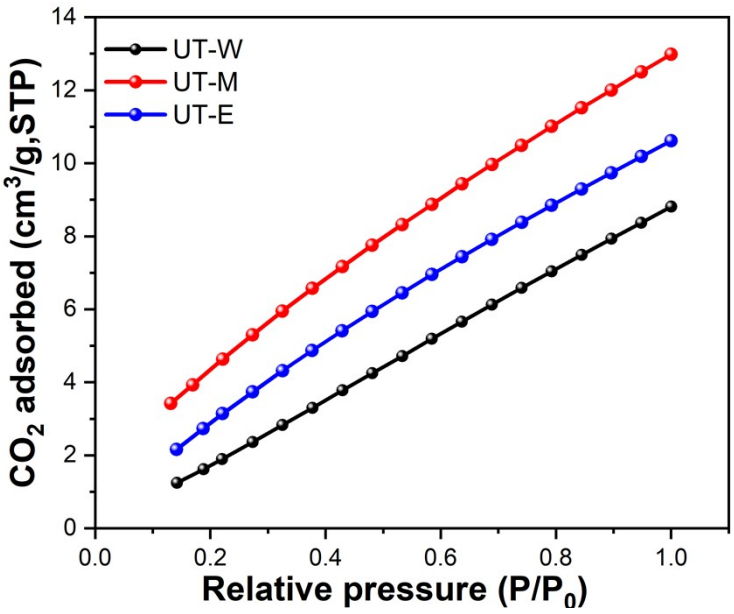

Figure S20 CO_2 adsorption isotherms at 298 K and 1 atm of UT-W, UT-M, and UT-E.

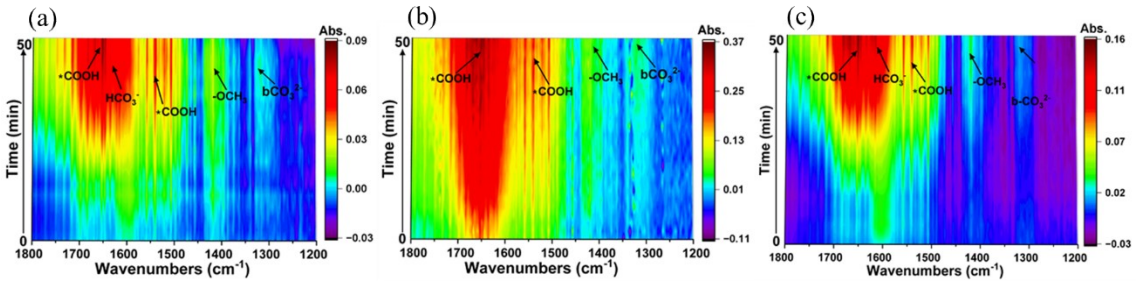

Figure S21 In-situ CO_2 adsorption DRIFTS spectra of (a) UT-W, (b) UT-M and (c) UT-E under the dark condition.

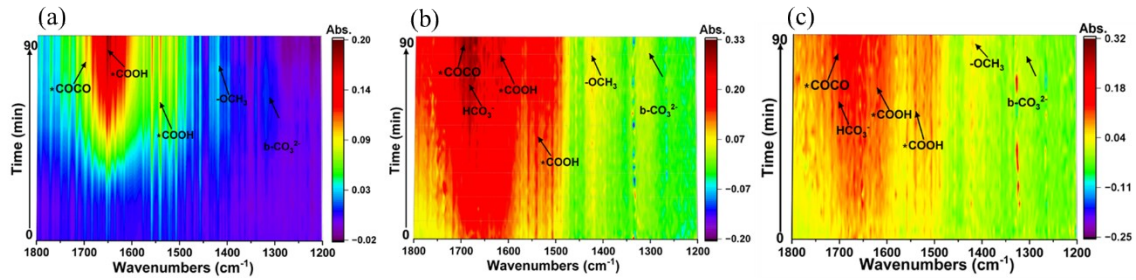

Figure S22 In-situ DRIFTS spectra of (a) UT-W, (b) UT-M, and (c) UT-E in the presence of CO_2 and H_2O vapor interaction taken at different irradiation time.

The IR bands at 1340 cm^{-1}, 1425cm^{-1}, 1685 cm^{-1} are assigned to the adsorbed b-CO_3^{2-}, *OCH_3, and HCO_3^-, respectively. Additionally, the bands at ~1542 cm^{-1}, 1619 cm^{-1}, and 1654 cm^{-1} were indexed to *COOH. Crucially, the key intermediate of *COCO is observed at ~1710 cm^{-1} and its intensity increased progressively with the irradiation time, indicating the production of the C2 products.

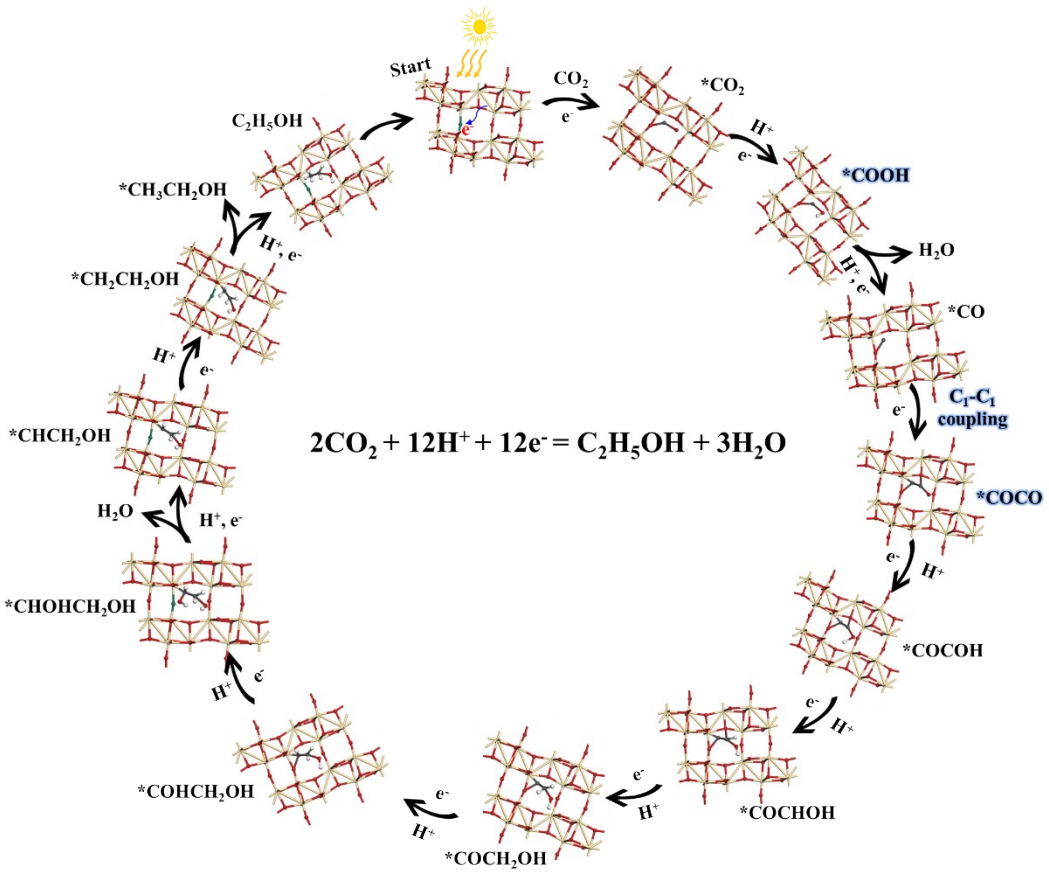

Figure S23 The possible reaction pathways for CO_2 reduction to ethanol on ultrathin TiO_2 nanosheets.

First, the O atom in CO_2 would be adsorbed on the O_v, and then reduced to *CO through *COOH intermediate. Second, the majority of *CO undergoes further coupling with another *CO to form *COCO on the surface of ultrathin TiO_2 nanosheets, which is the most important step for the generation of C2 product. Thirdly, the *COCO intermediate undergoes a series of hydrogenation to from the $*CH_2CH_2OH$. Finally, it dehydrates to C_2H_5OH.

Table S1-S5

Table S1 The results of N_2 adsorption and desorption experiment

Sample	Surface area ($m^2 \cdot g^{-1}$)	Pore volume ($cm^3 \cdot g^{-1}$)	Pore Size (nm)
UT-W	382.5	0.39	4.1
UT-M	413.3	0.42	4.0
UT-E	362.0	0.36	3.9

Table S2 Photocatalytic CO_2 reduction to liquid-phase for QE determination on UT-M catalyst

Catalyst	Time (h)	Wavelength (nm)	QE (CH_3OH) (%)	QE (C_2H_5OH) (%)
UT-M	8	365	8.7	18.3
		420	0.6	1.2
		450	0.2	0.5

Table S3 Comparison of photocatalytic performance in CO_2 reduction to liquid products on ultrathin TiO_2 nanosheets

Photocatalyst	Light source	Reaction medium	Liquid products yield ($\mu mol \bullet g^{-1} \bullet h^{-1}$)	Selectivity (%)	Refs
UT-M	300 W Xe	H_2O	CH_3OH: 20.8 C_2H_5OH: 37.2	77.0	This work
TiO_2	300 W UV-enchanced Xe	0.1 M $NaHCO_3$ solution	CH_3OH: 0.34 C_2H_5OH: 6.16	66.17	[2]
InCu/PCN	300 W Xe	DMF/H_2O	C_2H_5OH: 28.5	92.4	[3]
0.5% $Ni(OH)_2$-TiO_2	300 W Xe	H_2O	CH_3OH: 0.11 C_2H_5OH: 0.15	/	[4]
d-UiO-66/MoS-5 wt %	300 W Xe-arc ($\lambda > 400$ nm)	H_2O	CH_3COOH: 39.0 C_2H_5OH: 2.5	94	[5]
Carbon/TiO_2 hollow spheres	300 W Xe	H_2O	CH_3OH: 9.11	/	[6]
Cu/CN	300 W Xe	H_2O	CH_3OH: 1.75	/	[7]
Partially reduced Co_3O_4	300 W Xe	H_2O	CH_3COOH: 2.95	92.5	[8]
g-C_3N_4/CeO_2	300 W Xe ($\lambda > 420$ nm)	H_2O	CH_3OH: 5.2	33.6	[9]
STO/Cu@Ni/TiN	300 W Xe	H_2O	C_2H_5OH: 21.3	79	[10]
$BiVO_4$	300 W Xe	1.0 M NaOH solution	CH_3OH: 27.6	/	[11]
WS_2@Bi_2S_3	300 W Xe (780 nm > λ > 420 nm)	H_2O	CH_3OH: 9.55	/	[12]
Cu SAs/UiO-66-NH_2	300 W Xe ($\lambda > 400$ nm)	TEOA/H_2O	CH_3OH: 5.33 C_2H_5OH: 4.22	44.2	[13]
Vo-rich Zn $_2GeO_4$	300 W Xe	Simulated air in water	CH_3COH: 12.7	66.9	[14]

Table S4 The semi-quantitative analysis of three key intermediates of in-situ DRIFTS

	Products yield (μmol•g^{-1}•h^{-1})			**The IR intensities of three key intermediates**		
	CO	CH_3OH	C_2H_5OH	*COOH	*OCH_3	*COCO
UT-M	34.36	166.23	297.73	0.31	0.05	0.22
UT-E	11.63	128.93	242.71	0.14	0.04	0.18
UT-W	17.93	115.36	134.24	0.16	0.03	0.10

In order to visualize the relationship between the product yield of the samples and the IR intensities of the corresponding key intermediates, we list the ratios in the following table:

	CO yield	*COOH intensity	CH_3OH yield	*OCH_3 intensity	C_2H_5OH yield	*COCO intensity
θ1	2.95	2.21	1.29	1.25	1.23	1.22
θ2	1.92	1.94	1.44	1.67	2.22	2.20
θ3	0.65	0.88	1.12	1.33	1.81	1.80

Note: *θ1、θ2 and θ3 represent the ratio of UT-M to UT-E, the ratio of UT-M to UT-W, and the ratio of UT-E to UT-W, respectively.*

Table S5 The possible reaction pathways during photocatalytic CO_2 reduction to CO, CH_4, CH_3OH, and C_2H_5OH on ultrathin TiO_2 nanosheets on light illumination

Reaction pathway		
CO_2 (g) + e^- → *CO_2		
*CO_2 + e^- + H^+ → *COOH		
*COOH + e^- + H^+ → *CO + H_2O (l)		
*CO + *CO + e^- → *COCO	or	*CO → CO (g) + *
*COCO + e^- + H^+ → *COCOH		*CO + e^- + H^+ → *CHO
*COCOH + e^- + H^+ → *COCHOH		*CHO + e^- + H^+ → *CH_2O
*COCHOH + e^- + H^+ → *$COCH_2OH$		*CH_2O + e^- + H^+ → *CH_3O
*$COCH_2OH$ + e^- + H^+ → *$CHOCH_2OH$		*CH_3O + e^- + H^+ → *CH_3OH
*$CHOCH_2OH$ + e^- + H^+ → *$CHOHCH_2OH$		*CH_3OH + e^- + H^+ → CH_3OH (l) + e^- + *
*$CHOHCH_2OH$ + e^- + H^+ → *$CHCH_2OH$ + H_2O (l)		*CH_3O + e^- + H^+ → CH_4 (g) + H_2O + *
*$CHCH_2OH$ + e^- + H^+ → *CH_2CH_2O		
*CH_2CH_2OH + e^- + H^+ → *CH_3CH_2OH		
*CH_3CH_2OH → CH_3CH_2OH (l) + e^- + *		

References

1. T. Di, J. Zhang, B. Cheng, J. Yu and J. Xu, *Science China Chemistry*, 2018, **61**, 344-350.
2. M.-P. Jiang, K.-K. Huang, J.-H. Liu, D. Wang, Y. Wang, X. Wang, Z.-D. Li, X.-Y. Wang, Z.-B. Geng, X.-Y. Hou and S.-H. Feng, *Chem*, 2020, **6**, 2335-2346.
3. H. Shi, H. Wang, Y. Zhou, J. Li, P. Zhai, X. Li, J. J. Gurzadyan, Z. Hou, H. Yang and X. Guo, *Angew Chem Int Ed Engl*, 2022, **61**, e202208904.
4. A. Meng, S. Wu, B. Cheng, J. Yu and J. Xu, *Journal of Materials Chemistry A*, 2018, **6**, 4729-4736.
5. F. Yu, X. Jing, Y. Wang, M. Sun and C. Duan, *Angew Chem Int Ed Engl*, 2021, **60**, 24849-24853.
6. W. Wang, D. Xu, B. Cheng, J. Yu and C. Jiang, *Journal of Materials Chemistry A*, 2017, **5**, 5020-5029.
7. J. Wang, T. Heil, B. Zhu, C. W. Tung, J. Yu, H. M. Chen, M. Antonietti and S. Cao, *ACS Nano*, 2020, **14**, 8584-8593.
8. S. Zhu, X. Li, X. Jiao, W. Shao, L. Li, X. Zu, J. Hu, J. Zhu, W. Yan, C. Wang, Y. Sun and Y. Xie, *Nano Lett*, 2021, **21**, 2324-2331.
9. M. Liang, T. Borjigin, Y. Zhang, B. Liu, H. Liu and H. Guo, *Applied Catalysis B: Environmental*, 2019, **243**, 566-575.
10. H. Yu, C. Sun, Y. Xuan, K. Zhang and K. Chang, *Chemical Engineering Journal*, 2022, **430**, 132940.
11. J. Mao, T. Peng, X. Zhang, K. Li and L. Zan, *Catalysis Communications*, 2012, **28**, 38-41.
12. W. WS2 quantum dots seeding in Bi2S3 nanotubes: A novel Vis-NIR light sensitive photocatalyst with low-resistance junction interface for CO2 reductionDai, J. Yu, S. Luo, X. Hu, L. Yang, S. Zhang, B. Li, X. Luo and J. Zou, *Chemical Engineering Journal*, 2020, **389**, 123430.
13. G. Wang, C. T. He, R. Huang, J. Mao, D. Wang and Y. Li, *J Am Chem Soc*, 2020, **142**, 19339-19345.
14. J. Zhu, W. Shao, X. Li, X. Jiao, J. Zhu, Y. Sun and Y. Xie, *J Am Chem Soc*, 2021, **143**, 18233-18241.